Tin Oxides with Hollandite Structure as Anodes for Lithium Ion Batteries

N. Sharma,[†] J. Plévert,[‡] G. V. Subba Rao,[†] B. V. R. Chowdari,*[,†] and T. J. White[‡]

Department of Physics, National University of Singapore, Singapore 117542, and School of Materials Engineering, Nanyang Technological University, Singapore 639798

Received March 7, 2005. Revised Manuscript Received May 31, 2005

Tin oxides, $K_2(M,Sn)_8O_{16}$ (M = Li, Mg, Fe, or Mn), possessing the hollandite crystal structure have been synthesized and characterized by a variety of techniques, and their electrochemical behavior was studied. The compounds $K_2(Li_{2/3}Sn_{22/3})O_{16}$ (K−Li), $K_2(Mn_2Sn_6)O_{16}$ (K−Mn), and $K_2(Fe_2Sn_6)O_{16}$ (K−Fe) are new phases. Rietveld refinement of the powder X-ray diffraction data showed that these Sn-hollandites exhibit a simple tetragonal structure. X-ray photoelectron spectroscopy on (K−Li) and (K−Mg) confirm formal valencies of the ions in the compounds. Galvanostatic cycling versus Li metal in the voltage range of 0.005−1.0 V at the current density of 60 mA/g showed the first cycle charge capacities of 602, 505, 481, and 418 (± 3) mAh/g for (K−Li), (K−Mg), (K−Fe), and (K−Mn), respectively. These values correspond to 3.7−3.0 mol of recyclable Li/mol of Sn. At the end of 50 cycles, (K−Li) and (K−Fe) performed better and retained 78 and 83% of the initial capacity. The (K−Li) also showed good rate capability. The Coulombic efficiency was >98% between 10 and 50 cycles in all cases except (K−Mn) with the average charge and discharge voltages of 0.4−0.5 and 0.25−0.3 V, respectively. Cyclic voltammograms complement the galvanostatic results. Impedance spectral data on the (K−Li) versus Li at different voltages during the 1st and 15th discharge−charge cycle have been analyzed and interpreted.

1. Introduction

Binary and ternary oxides of tin (Sn) in glassy, amorphous, and crystalline forms have been extensively studied as alternate materials to the commercially employed graphite as anodes for lithium ion batteries (LIB).[1−4] The reversible capacity in them arises as a result of de-alloying/alloying reaction of $Li_{4.4}Sn$ at voltages 0.3−0.5 V versus Li. This reaction, however, causes volume variations and thus mechanical stresses in the electrode leading to capacity fading. This issue has been addressed during the last 8 yr through various strategies, and the key factors influencing the attainable capacity and its stability to long-term cycling have been enumerated: the nature and amount of counter (matrix) atoms/ions that are electrochemically inactive, the starting crystal structure and oxygen coordination of tin in the compound, particle size and morphology, and the operating voltage range versus Li. Some examples pertaining to these findings are the tin oxides in glassy matrix (Sn_2BPO_6, $Sn_2P_2O_7$, $SnMn_{0.5}PO_4$, $SnB_xP_yO_z$, $Sn_2B_2O_5$)[5−12] and in crystalline form (SnO, $CoSnO_3$, $Sn_2O_3(OH)_2$, SnP_2O_7, M_2SnO_4 (M = Mn, Mg, Co), $CaSnO_3$, Ca_2SnO_4, and $NaFeSnO_4$).[13−23]

Investigations on M_2SnO_4[17,18] having SnO_4 tetrahedra with the inverse-spinel structure and M countercation as the matrix showed that the first-discharge plateau occurs at 0.1 and 0.7 V versus Li for M = Mg and Mn respectively in comparison to 0.9 V plateau of the SnO_2. Furthermore, the first-cycle reversible capacity was smaller than that of SnO_2, which has SnO_6 octahedra and tetragonal rutile structure. It was inferred

* Corresponding author. Tel.: +65 6874 2956. Fax: +65 6777 6126. E-mail: phychowd@nus.edu.sg.
[†] National University of Singapore.
[‡] Nanyang Technological University.

(1) Winter, M.; Besenhard, J. O. *Electrochim. Acta* **1999**, *45*, 31.
(2) Tarascon, J. M.; Armand, M. *Nature* **2001**, *414*, 359.
(3) Schalkwijk, W. A. V., Scrosati, B., Eds. In *Advances in Lithium-Ion Batteries*; Kluwer Academic/Plenum: New York, 2002.
(4) Nazri, G. A., Pistoia, G., Eds. *Lithium Batteries, Science and Technology*; Kluwer Academic: New York, 2003.
(5) Idota, Y.; Kubota, T.; Matsufuji, A.; Maekawa, Y.; Miyasaka, T. *Science* **1997**, *276*, 1395.
(6) Machill, S.; Shodai, T.; Sakurai, Y.; Yamaki, J. *J. Power Sources* **1998**, *73*, 216.
(7) Machill, S.; Shodai, T.; Sakurai, Y.; Yamaki, J. *J. Solid State Electrochem.* **1999**, *3*, 97.
(8) Wan, K.; Li, S. F. Y.; Gao, Z.; Siow, K. S. *J. Power Sources* **1998**, *75*, 9.
(9) Lee, J. Y.; Xiao, Y.; Liu, Z. *Solid State Ionics* **2000**, *133*, 25.
(10) Nazar, L. F.; Goward, G.; Leroux, F.; Duncan, M.; Huang, H.; Kerr, T.; Gaubicher, J. *Int. J. Inorg. Mater.* **2001**, *3*, 191.
(11) Courtney, I. A.; Dahn, J. R. *J. Electrochem. Soc.* **1997**, *144*, 2943.
(12) Courtney, I. A.; McKinnon, W. R.; Dahn, J. R. *J. Electrochem. Soc.* **1999**, *146*, 59.
(13) Courtney, I. A.; Dahn, J. R. *J. Electrochem. Soc.* **1997**, *144*, 2045.
(14) Huang, F.; Yuan, Z.; Zhan, H.; Zhou, Y.; Sun, J. *Mater. Lett.* **2003**, *57*, 3341.
(15) Kim, J.-H.; Jeong, G.-J.; Kim, Y.-W.; Sohn, H. J.; Park, C. W.; Lee, C. K. *J. Electrochem. Soc.* **2003**, *150*, A1544.
(16) Behm, M.; Irvine, J. T. S. *Electrochim. Acta* **2002**, *47*, 1727.
(17) Connor, P. A.; Irvine, J. T. S. *J. Power Sources* **2001**, *97*−*98*, 223.
(18) Connor, P. A.; Irvine, J. T. S. *Electrochim. Acta* **2002**, *47*, 2885.
(19) Sharma, N.; Shaju, K. M.; Subba Rao, G. V.; Chowdari, B. V. R. *Electrochem. Commun.* **2002**, *4*, 947.
(20) Sharma, N.; Shaju, K. M.; Subba Rao, G. V.; Chowdari, B. V. R. In *Solid State Ionics: Trends in The New Millennium*; Chowdari, B. V. R., Prabaharan, S. R. S., Yahaya, M., Talib, I. A., Eds.; World Scientific: Singapore, 2002; p 87.
(21) Sharma, N.; Subba Rao, G. V.; Chowdari, B. V. R. In *Solid State Ionics: The Science and Technology of Ions in Motion*; Chowdari, B. V. R., Yoo, H.-I., Choi, G. M., Lee J. H., Eds.; World Scientific: Singapore, 2004; p 411.
(22) Sharma, N.; Shaju, K. M.; Subba Rao, G. V.; Chowdari, B. V. R. *J. Power Sources* **2005**, *139*, 250.
(23) Sharma, N.; Shaju, K. M.; Subba Rao, G. V.; Chowdari, B. V. R. *J. Power Sources* **2003**, *124*, 204.

10.1021/cm0505042 CCC: $30.25
Published on Web 08/10/2005

that, apart from the main electrochemically active Sn ion, the discharge characteristics and reversible capacities are a function of the counterion as well. Our studies on the tin compounds $ASnO_3$, A = Ca, Sr, Ba with the perovskite structure,[19−22] Ca_2SnO_4 (Sr_2PbO_4 structure),[22] and $NaFeSnO_4$ ($CaFe_2O_4$ –related structure)[23] revealed that Na, Ca, and Fe are the beneficial matrix elements that help in the suppression of capacity fading. Furthermore, compounds with the perovskite structure, especially $CaSnO_3$ consisting of corner-linked SnO_6 octahedra perform much better than those with other structures in giving high and stable capacities. Studies by Behm and Irvine[16] on SnP_2O_7 possessing two different crystal structures clearly indicated that the cubic phase with the isolated SnO_6 octahedra (and corner-linked to the PO_4 tetrahedra) showed high reversible capacity and 96% capacity retention after 50 cycles, whereas SnP_2O_7 with the layered structure, which may not contain such isolated SnO_6 species, showed a low initial capacity and only 53% capacity retention after 50 cycles.

Thus, the starting crystal structure of the Sn compound and SnO_y coordination polyhedra play a very important role in determining the cycling performance. The perovskite or other network structures containing only corner-linked or isolated SnO_6 octahedra appear to be the "favorable" structures. This may seem surprising at first since the crystal structure of the compound gets destroyed during the first-discharge reaction with Li. However, it should still strongly influence the local structure of the resulting non-crystalline or nano-crystalline lithiated material, which also contains the matrix metal/ion and affect the electrochemistry of Li de-insertion/insertion. As pointed out by Behm and Irvine[16] and Connor and Irvine,[17] there is a need for continued search for the optimum crystal structure, matrix element, and its composition to realize the best performance.

Tin oxides containing SnO_6 octahedra are encountered in compounds with the hollandite structure, $A_x(M,Sn)_8O_{16}$, where A is a large-size cation like Ba or K, $x \leq 2$. The M is a countercation with a valency of 2+ or 3+ and provides the charge balance for the compound.[24−30] The hollandites $Ba(M^{3+}{}_2Sn^{4+}{}_6)O_{16}$, M = Ga, In, Cr,[25,26] $K_2(Ga_2Sn_6)O_{16}$,[27] and, recently, $K_2(Mg^{2+}Sn_7)O_{16}$[28] have been prepared and studied for possible use as catalysts and gas sensors. The hollandites crystallize with a tetragonal symmetry, but depending on the A and (M, Sn) ions, monoclinic distortion is also observed.[24−28] The structure consists of double chains of edge-shared $(M,Sn)O_6$ octahedra that are connected at their corners to form a framework of 1D channels with the 8-fold O-coordination (Figure 1). These so-called 2 × 2 octahedra channels are occupied by the A-cations, represented by filled circles in Figure 1. The versatile nature of the structure allows Sn^{4+} ion to be replaced by other cations such as Ti, V, Cr, Mn, Mo, or Ru, and the M ion can also be Li^+.[24−26,29,30] Presently, we synthesized and characterized the phases $K_2(Li_{2/3}Sn_{22/3})O_{16}$, $K_2(MgSn_7)O_{16}$, and $K_2(M^{3+}{}_2Sn^{4+}{}_6)O_{16}$, M = Mn and Fe. These compounds were studied for their electrochemical behavior toward Li metal and to find out their applicability as anodes for LIB.

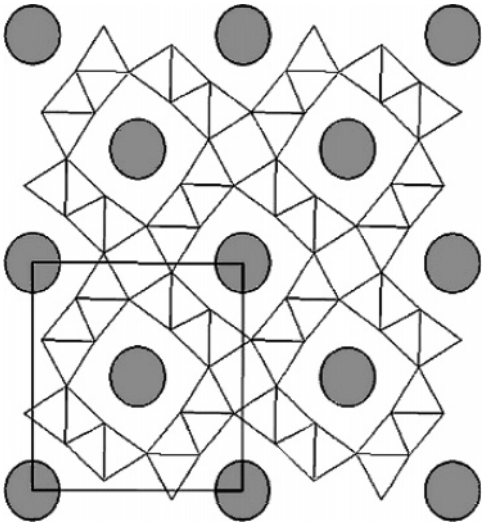

Figure 1. Structure of hollandite tin oxide, $K_2(M,Sn)_8O_{16}$, projected along the *c* axis showing the double chains of edge-shared $(M,Sn)O_6$ octahedra that are connected at their corners to form a framework of 1D channels (2 × 2 octahedra) with the 8-fold O-coordination. Filled circles represent the K cations occupying the channels. The unit cell is represented by lines.

2. Experimental Section

The compound $K_2(MgSn_7)O_{16}$ was synthesized by the conventional solid-state method reported by Uheda et al.[28] The stoichiometric mixture of K_2CO_3 (BDH), $Mg(NO_3)_2{\cdot}6H_2O$ (Merck), and SnO_2 (Merck) to give ~10 g of the product was finely ground in an autogrinder, and the powder was pressed into a pellet. It was then subjected to a series of heat treatments in air for 5 h each in a box furnace (Carbolite, UK) at 600, 900, and 1150 °C with intermittent cooling to room temperature, grinding, and pelletizing at each stage. Heating and cooling rates were 3 °C/min. Other three compounds, $K_2(Li_{2/3}Sn_{22/3})O_{16}$, $K_2(Fe_2Sn_6)O_{16}$, and $K_2(Mn_2Sn_6)O_{16}$, were also prepared by the same method using Li_2CO_3 (Merck)/Fe_2O_3 (Fischer)/$(CH_3COO)_2Mn{\cdot}4H_2O$ (Acoros, USA).

X-ray powder diffraction data were collected using a Bruker D5005 diffractometer with Cu Kα radiation, equipped with a graphite monochromator and Soller slits. A step scan was performed over a 2θ range of 10−150°, with a step size $\Delta 2\theta = 0.02°$, and a counting time of about 10 s per step. The Rietveld refinements of the powder data were performed using the GSAS software package.[31] Surface morphology was examined using SEM (JEOL JSM-6700F, field emission electron microscope). The BET surface area of the hollandite powders was measured by Micromeritics Tristar 3000 (USA). Density measurements have been done on $K_2(Li_{2/3}Sn_{22/3})O_{16}$ and $K_2(MgSn_7)O_{16}$ by the helium displacement method using Micromeritics pycnometer, model accupyc 1330. X-ray photoelectron spectroscopy of the compounds was carried out with the VG Scientific ESCA MK II spectrometer (Mg Kα radiation).

(24) Kesson, S. E.; White, T. J. *J. Solid State Chem.* **1986**, *63*, 122.
(25) Kesson, S. E.; White, T. J. *Proc. R. Soc. London* **1986**, *A408*, 295.
(26) Zandbergen, H. W.; Everstijn, P. L. A.; Mijlhoff, F. C.; Renes, G. H.; Ijdo, D. J. W. *Mater. Res. Bull.* **1987**, *22*, 431.
(27) Fujimoto, K.; Watanabe, M.; Mori, T.; Ito, S. *J. Mater. Res.* **1998**, *13*, 926.
(28) Uheda, K.; Horiuchi, A.; Takizawa, H.; Endo, T. *J. Porous Mater.* **1999**, *6*, 161.
(29) Marimuthu, K. N.; Smart, L. E.; Berry, F. J.; Varadaraju, U. V. *Mater. Chem. Phys.* **2003**, *82*, 672.
(30) Fan, W.; Ding, J.; Yi, J. B.; Rao, G. V. S.; Chowdari, B. V. R. *J. Magn. Magn. Mater.* **2004**, *272*, e1801.
(31) Larson, A. C.; Von Dreele, R. B. *Generalized Structure Analysis System*; *Report LAUR 86-748*; Los Alamos National Laboratory: Los Alamos, NM, 1990.

The high-resolution spectra were recorded with a constant pass energy mode (20 eV). Charge referencing was done against the adventitious carbon, C 1s, with the known binding energy (BE) = 284.6 eV. The raw spectra were curve-fitted using XPS peak fit software. Wherever necessary, the spectra were delineated by nonlinear least-squares fitting with a Gauss−Lorentz (ratio 60:40) curve into multiple peaks, and the corresponding BEs were evaluated. The BEs are accurate to ±0.1 eV.

The electrochemical studies on the compounds were done with respect to Li metal in the form of coin cell using the oxides as cathodes. The electrodes were fabricated using a mixture of active material, Super P carbon, and binder (Kynar 2801) in the weight ratios, 70:15:15 using 1-methyl 2-pyrrolidone (NMP) as the mixing medium. A thick and uniform slurry of this was coated onto an etched copper foil by the doctor blade technique. Drying at 80 °C in an air oven for 24 h evaporated the NMP. The dried thick film (20−30 μm) electrodes were pressed between twin rollers prior to cutting in to circular disks (16 mm). After drying in a vacuum oven at 70 °C for 12 h, these were transferred to an Ar-filled glovebox, which maintains <1 ppm of H_2O and O_2 (MBraun, Germany). Coin cells (size 2016) were fabricated in the glovebox. The other cell components were Li metal (Kyokuto Metal Co., Japan) foil as counter electrode, Celgard 2502 membrane as the separator, and 1 M $LiPF_6$ in ethylene carbonate (EC) and diethyl carbonate (DEC) (1:1 by volume, Merck Selectipur LP40) as the electrolyte. The active material in the composite electrode ranged from 5 to 7 mg. Nominal electrode surface area is 2.0 cm^2. The cells were aged for 24 h before testing. The cyclic voltammetry and galvanostatic charge−discharge cycling of the cells were carried out at room temperature (RT = 25 °C) by a computer-controlled MacPile II (Biologic, France) unit and a Bitrode multiple battery tester (model SCN, Bitrode, USA). Electrochemical impedance spectroscopy was done using the Solartron Impedance/Gain-Phase Analyzer (SI 1260) coupled with a Battery Test Unit (1470). An ac signal with amplitude of 5 mV at the frequency varying from 0.35 MHz to 2 mHz was used to measure the impedance response. Data acquisition and analysis were done respectively using the electrochemical impedance software ZPlot and Zview (Version 2.2, Scribner Associates Inc., USA).

3. Results and Discussion

3.1. Structure and Morphology. The compounds $K_2(MgSn_7)O_{16}$ (hereafter, (K−Mg)) and $K_2(Li_{2/3}Sn_{22/3})O_{16}$ (K−Li) are white whereas $K_2(Fe_2Sn_6)O_{16}$ (K−Fe) and $K_2(Mn_2Sn_6)O_{16}$ (K−Mn) are dark yellow and brown, respectively. The newely synthesized isostructural phases are (K−Li), (K−Fe), and (K−Mn). The XRD patterns of (K−Li), (K−Fe), and (K−Mn) are shown in Figure 2a−c. The patterns are similar and resemble those of (K−Mg) (not shown in Figure 2). Rietveld refinement of the diffraction data was done on all the compounds on the basis of hollandite structure with tetragonal symmetry and space group, *I*4/*m* (no. 87). A second phase, present as trace in the samples of (K−Li), (K−Mg), and (K−Mn) and identified as cassiterite-SnO_2 was incorporated into the structure refinement. The (K−Mn) phase contains, in addition to SnO_2, some small unidentified peaks. The diffraction peaks of the main phase were modeled using a pseudo-Voigt profile function that includes an anisotropic particle size broadening contribution. Preferred orientation terms were added in to the refinement. The fractional occupancies of the Sn/M sites were fixed whenever possible to respect the charge neutrality of the structures. Crystallographic information and atomic coordinates are given in Table 1.

The refinement of the hollandite compounds showed their nominal composition and therefore reasonable *R* factors for both the structure and profile fitting (Table 1), thereby giving some justification, in our case, for not selecting a monoclinic subgroup as reported by Uheda et al. for (K−Mg).[28] In the three compounds, the potassium cation is located in one site only but shows a large thermal factor, suggesting possible disorder/modulation of the structures. The potassium site is 8-coordinated. In (K−Fe), the distance K−O1 is about 3.103(6) Å; in (K−Li) and (K−Mg), the distances are 3.130(6) and 3.151(6) Å, respectively. Based on bond valence calculation, the site is not favorable for potassium in all three structures as its dimensions are too large for the cation. The Sn(M) octahedra are slightly distorted in similar manners in the three structures. For (K−Fe), the six distances Sn(Fe)-O vary from 2.013(8) to 2.091(4) Å with a mean distance 2.054 Å. The mean distances Sn(Li)-O and Sn(Mg)-O are 2.070 and 2.059 Å, respectively. The incorporation of M ion at the Sn site is clearly reflected in the tetragonal *a* lattice parameters and the unit cell volumes (*V*). The *a* and *V* values decrease with the decreasing tin content from 7.34 → 7 → 6 in the compounds (K−Li), (K−Mg), and (K−Fe)/(K−Mn), respectively. The variation in *a* value also proves indirectly that little, if any, Li ions occupy the rutile-type 1 × 1 octahedra channels in the hollandite structure.

The SEM photographs of the hollandite compounds indicate qualitative resemblance between (K−Mg) and (K−Li) with the former having some what smaller particle size (submicron) than the latter (Figure 3a,b). The compounds (K−Fe) and (K−Mn) comprised aggregates of small particles and have higher degree of nonuniformity in particle morphology (not shown in Figure 3). The BET surface areas of the hollandites (K−M), M = Mg, Li, Fe, Mn are 2.6, 1.4, 0.8, and 0.9 (± 0.02) m^2/g, respectively, thus reaffirming the small particle size of (K−Mg). The experimental densities of the compounds (K−Mg) and (K−Li) were found to be 5.817 and 5.756 g/cm^3, respectively. These values are close to the theoretical X-ray densities. The difference (∼1−3%) may be explained by the presence of traces of SnO_2 detected in both compounds by XRD.

3.2. XPS of Hollandites. The X-ray photoelectron spectroscopy (XPS) is a nondestructive but surface-sensitive technique that provides information pertaining to the elemental composition of a compound and the oxidation states of the elements. The XPS of tin hollandites have not been reported in the literature. Figure 4 shows XPS spectra for the compounds $K_2(MgSn_7)O_{16}$ (K−Mg) and $K_2(Li_{2/3}Sn_{22/3})O_{16}$ (K−Li) in various BE regions. Since Li and Mg are present in small amounts in comparison to K, Sn, and O, the XPS signal-to-noise ratio corresponding to these elements was very weak and not shown in Figure 4. The K 2p core level spectra of (K−Mg) and (K−Li) shown in Figure 4a,b comprise two overlapped peaks in the range 290−297 eV corresponding to K $2p_{3/2}$ and K $2p_{1/2}$ with a peak separation, $\Delta = (2p_{3/2} - 2p_{1/2}) = 2.8$ eV for both the compounds. The K $2p_{3/2}$ peak positions for K (metal), KOH, KO_2, K_2O_2, and

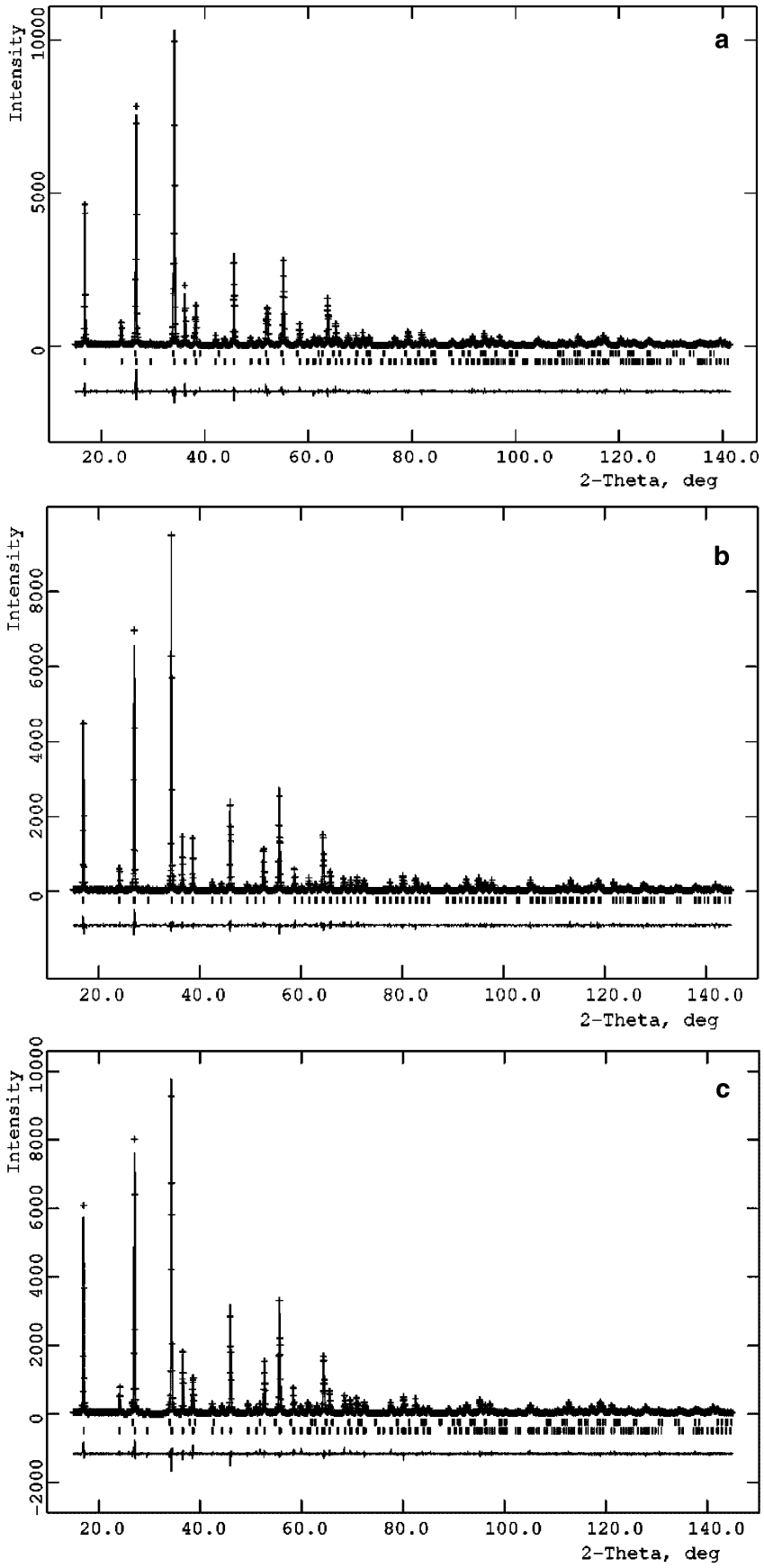

Figure 2. Observed and calculated (Rietveld refined) X-ray powder diffraction patterns of tin hollandites. (a) $K_2(Li_{2/3}Sn_{22/3})O_{16}$ (K−Li), (b) $K_2(Fe_2Sn_6)O_{16}$ (K−Fe), and (c) $K_2(Mn_2Sn_6)O_{16}$ (K−Mn). The difference curve is plotted, and the allowed reflections are indicated by vertical bars. Second set of vertical bars in panels a and c correspond to the allowed reflections for cassiterite-SnO_2.

Table 1. Crystallographic and Refinement Data for Tin-Hollandites $K_2M_xSn_{(8-x)}O_{16}$ [a]

chemical formula	$K_2M_xSn_{8-x}O_{16}$	$K_2MgSn_7O_{16}$	$K_2Li_{0.66}Sn_{7.34}O_{16}$	$K_2Fe_2Sn_6O_{16}$	$K_2Mn_2Sn_6O_{16}$
cell parameters	a (Å)	10.4985(2)	10.5401(1)	10.4422(5)	10.4297(1)
	c (Å)	3.1694(1)	3.1648(1)	3.1456(1)	3.1604(1)
cell volume	V (Å^3)	349.33(2)	351.59(1)	343.00(3)	343.79(1)
R factors	R_F (%)[b]	2.1	2.0	2.0	3.5
	Rwp[c]	12.5	11.5	12.3	12.0
	GOF[d]	1.32	1.30	1.19	1.30
K 2(b)	$x = y$	0	0	0	0
	z	1/2	1/2	1/2	1/2
	U_{iso} (100 Å^2)	7.3(4)	9.9(4)	8.1(3)	18.2(6)
	occupancy	1	1	1	1
Sn/M 8(h)	x	0.3494(1)	0.3494(1)	0.3496(1)	0.3489(1)
	y	0.1653(1)	0.1658(1)	0.1654(1)	0.1646(1)
	z	0.0	0.0	0.0	0.0
	U_{iso} (100 Å^2)	0.60(2)	0.63(2)	0.44(2)	0.71(2)
	occupancy (Sn)	0.875	0.917	0.75	0.75
	occupancy (M)	0.125	0.083	0.25	0.25
O1 8(h)	x	0.1555(7)	0.1553(7)	0.1566(6)	0.1598(6)
	y	0.2076(7)	0.2038(7)	0.2028(6)	0.2038(6)
	z	0.0	0.0	0.0	0.0
	U_{iso} (100 Å^2)[e]	0.3(1)	0.5(1)	0.5(1)	0.8(1)
O2 8(h)	x	0.5431(9)	0.5427(8)	0.5423(8)	0.5444(8)
	y	0.1689(8)	0.1665(7)	0.1670(7)	0.1699(7)
	z	0.0	0.0	0.0	0.0
	U_{iso} (100 Å^2)[e]	0.3(1)	0.5(1)	0.5(1)	0.8(1)

[a] Crystal system, tetragonal; space group $I4/m$; number of formula units per unit cell, Z = 1. [b] $R_F = \Sigma|F_o - F_c|/\Sigma F_o$. [c] Rwp = $\sqrt{\Sigma w_i(y_{io}-y_{ic})^2/\Sigma w_i y_{io}^2}$. [d] GOF = $\sqrt{\Sigma w_i(y_{io}-y_{ic})^2/(N_{obs}-N_{var})}$. [e] U_{iso} for the oxygen atoms are constrained to have the same values.

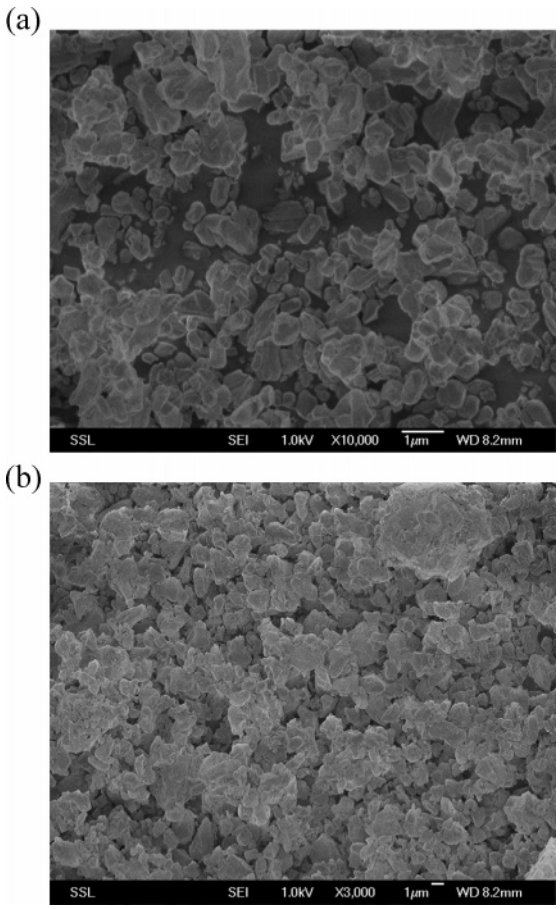

Figure 3. SEM photographs of the as-prepared tin hollandite powders. (a) $K_2(MgSn_7)O_{16}$ (K−Mg); (b) $K_2(Li_{2/3}Sn_{22/3})O_{16}$ (K−Li). Bar scale, 1 μm.

$KFeO_2$ are in the range of 292.8−294.7 eV.[32] The BE values of 292.5 and 292.3 eV observed for (K−Mg) and (K−Li) are comparable to the BE value of 292.7 eV for K $2p_{3/2}$ observed in $K^{1+}Fe^{3+}O_2$ (orthorhombic structure).[32]

The Sn 3d spectra (Figure 4c,d) for (K−Mg) and (K−Li) also comprise two peaks with BEs at 485.9 and 494.3 (± 0.1) eV attributable to Sn $3d_{5/2}$ and Sn $3d_{3/2}$, respectively. The peak separation $\Delta = 8.4$ eV for both the compounds. These observed BE values are comparable to those in $ASnO_3$ (A = Ca, Sr, Ba)[22] having Sn in octahedral O-coordination and 4+ oxidation state. The XPS in the O 1s region for (K−Mg) and (K−Li) are shown in Figure 4e,f. The observed asymmetric peak was fitted in to two overlapped peaks with BEs at 529.7 and 530.9 (± 0.1) eV for both the compounds. The O 1s peak at 529.7 eV can be ascribed to the O^{2-} arising from the hollandite anionic framework, and the low intensity peak at 530.9 eV is due to the OH^- and/or adsorbed oxygen.[22,33,34]

3.3. Galvanostatic Cycling of the Sn-Hollandites. The voltage versus capacity profiles of the first cycle in the galvanostatic cycling mode for the hollandites, (K−M), M = Li, Mg, Mn, Fe as cathodes versus Li were recorded at 60 mA/g and for (K−Li) also at the 100 mA/g current density. The curves shown in Figure 5a indicate that in all cases the first-discharge commences cathodically from the open circuit voltage (OCV = 2.6−2.8 V) up to 0.005 V followed by the charge curve up to the cutoff voltage, 1.0 V. For all the compounds the voltage drops rapidly from OCV to ∼0.8 V. Thereafter, the voltage plateau region (0.75−0.85 V) sets in. For (K−Mg) and (K−Li) the aforesaid region extends up to 400 mAh/g (∼17 mol of Li per formula unit) while for (K−Fe) and (K−Mn), the voltage plateau is stretched up to 600 mAh/g (∼26 mol of Li per formula unit). The plateau regions are followed by continuous sloping voltage profile up to 0.005 V. The total first-discharge

(32) Joseph, Y.; Ketteler, G.; Kuhrs, C.; Ranke, W.; Weiss, W.; Schlogl, R. *Phys. Chem. Chem. Phys.* **2001**, *3*, 4141.
(33) Manorama, S. V.; Gopal Reddy, C. V.; Rao, V. J. *Appl. Surf. Sci.* **2001**, *174*, 93.
(34) Machkova, M.; Brashkova, N.; Ivanov, P.; Carda, J. B.; Kozhukharov, V. *Appl. Surf. Sci.* **1997**, *119*, 127.

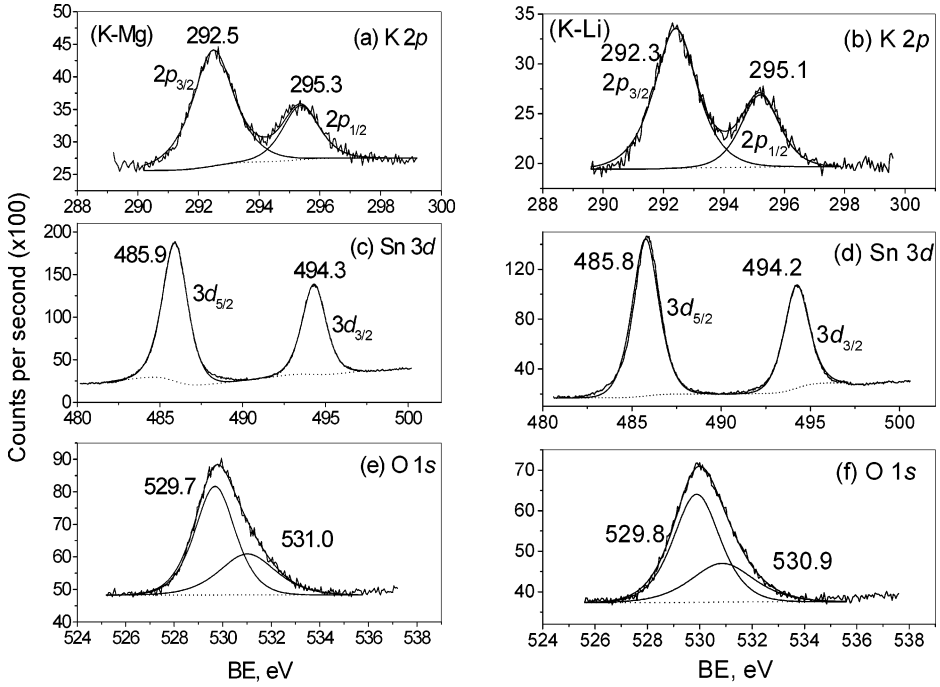

Figure 4. XPS spectra of $K_2(MgSn_7)O_{16}$ (K−Mg) and $K_2(Li_{2/3}Sn_{22/3})O_{16}$ (K−Li). (a) and (b) K 2p spectra; (c) and (d) Sn 3d spectra; (e) and (f) O 1s spectra. Baseline and curve-fitting of the raw data are shown. The numbers refer to binding energies (BE, ±0.1 eV).

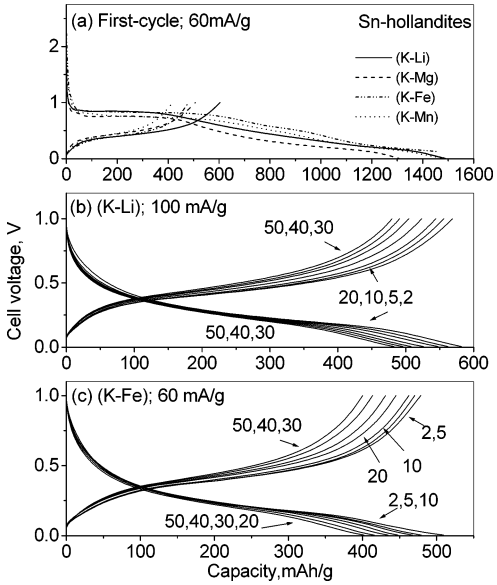

Figure 5. Voltage vs capacity profiles for the tin-hollandites. (a) First discharge−charge cycle from open circuit voltage (OCV) to 0.005 V vs Li at 60 mA/g. (b) $K_2(Li_{2/3}Sn_{22/3})O_{16}$ (K−Li) at 100 mA/g. (c) $K_2(Fe_2Sn_6)O_{16}$ (K−Fe) at 60 mA/g, 2−50 cycles in the voltage range, 0.005−1.0 V. Only select cycles are shown. Numbers refer to cycle numbers. (K−Mg) and (K−Mn) correspond to $K_2(MgSn_7)O_{16}$ and $K_2(Mn_2Sn_6)O_{16}$ respectively.

capacities for (K−Mg), (K−Li), (K−Fe), and (K−Mn) were found to be 1306, 1488, 1460, and 1487 mAh/g, respectively (Table 2 and Figure 5a). The minor differences in the voltage plateau positions are attributable to subtle effects of the nature of the M element in these hollandite compounds.

As has already been established in the other binary and ternary tin oxides,[1,2,6−23] in the above cases too, the first-discharge reaction is the crystal structure destruction process, leading to the formation of electrochemically active tin metal nanoparticles in an amorphous matrix of K_2O, Li_2O, and MgO/Mn/Fe-metal where in 28−30.8 mol of Li/formula unit will get consumed depending on Sn content and M ion. The reaction of (K−Mg) with Li, as an example, is given in eq 1. Further reaction with Li causes the Li−Sn alloy formation consuming 4.4 mol of Li/mol of Sn (eq 2):

$$K_2(MgSn_7)O_{16} + 28Li^+ + 28e^- \rightarrow K_2O + MgO + 7Sn + 14Li_2O \quad (1)$$

$$7Sn + 30.8\ Li^+ + 30.8e^- \leftrightarrow 7Li_{4.4}Sn \quad (2)$$

The plateau regions indicative of structure destruction consumed ∼17 mol of Li (∼400 mAh/g) for (K−Mg) and (K−Li) as against the expected 28.0 and 29.3 mol of Li. The K and Mg ions will not be reduced to metals due to their high K−O and Mg−O bond energies.[17,19,22,35] Similarly, for the (K−Fe) and (K−Mn) compounds, the plateau region corresponds to 26 mol of Li (∼600 mAh/g) instead of the theoretical amount of 30 mol of Li, assuming that the transition metal ions (Fe and Mn) are also reduced to the metals. The sloping voltage regions covering the large portion of the voltage-capacity profiles are indicative of the simultaneous occurrence of the two processes, viz., the structure destruction and the Li−Sn alloy formation. The theoretically expected first-discharge capacities along with the observed values and the equivalent number of moles of Li calculated from the respective molecular weights are given in Table 2. For convenience, the number of moles of recyclable Li/mole of Sn in the compounds are also given in Table 2. As can be seen, except the compound (K−Mg), all the other hollandites consumed slightly more moles of Li than the calculated amount, by 3−13%, during the first-discharge. This can be explained as due to the formation of the solid electrolyte interface (SEI) on the amorphous oxide matrix by the reaction of Li with the electrolyte. In the case of (K−

(35) Sharma, N.; Shaju, K. M.; Subba Rao, G. V.; Chowdari, B. V. R.; Dong, Z. L.; White, T. J. *Chem. Mater.* **2004**, *16*, 504.

Table 2. Theoretical and Observed Capacities (Corresponding Number of mol of Li/Formula Unit) and {mol of Recyclable Li/mol of Sn} for the Tin-Hollandites[a]

compd (mol wt) (code)	theor. capacity, mAh/g (mol of Li)		observed capacity (±3 mAh/g)						
	1st discharge	reversible capacity {4.4}	1st discharge	1st charge	20th discharge	20th charge	50th discharge	50th charge	capacity retention (%) (1−50 cycles)
$K_2(Li_{2/3}Sn_{22/3})O_{16}$; (1209 g) (K−Li)	1365(61.6)	716(32.3)	1488 (67.1)	602(27.2) {3.7}	551(24.9) {3.4}	548(24.7) {3.4}	472(21.3) {2.9}	472(21.3) {2.9}	78
$K_2(MgSn_7)O_{16}$; (1189 g) (K−Mg)	1325(58.8)	694(30.8)	1306(58.0)	505(22.4) {3.2}	442(19.6) {2.8}	439(19.5) {2.8}	344(15.3) {2.2}	343(15.2) {2.2}	68
$K_2(Fe_2Sn_6)O_{16}$; (1158 g) (K−Fe)	1305(56.4)	611(26.4)	1460(63.1)	481(20.8) {3.5}	448(19.4) {3.2}	445(19.2) {3.2}	401(17.3) {2.9}	400(17.3) {2.9}	83
$K_2(Mn_2Sn_6)O_{16}$; (1156 g) (K−Mn)	1307(56.4)	612(26.4)	1487(64.2)	418(18.0) {3.0}	259(11.2) {1.9}	257(11.1) {1.9}	222(9.6) {1.6}	221(9.5) {1.6}	53

[a] Voltage range, 0.005−1.0 V vs Li at the current density, 60 mA/g.

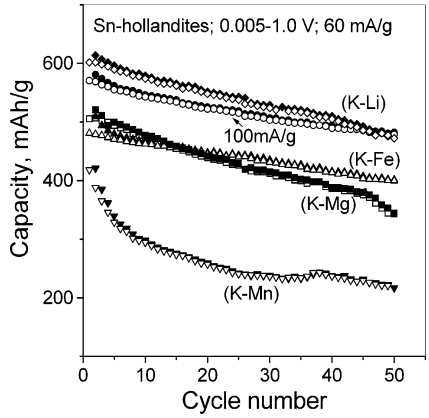

Figure 6. Capacity vs cycle number plots for $K_2(MgSn_7)O_{16}$ (K−Mg), $K_2(Li_{2/3}Sn_{22/3})O_{16}$ (K−Li), $K_2(Fe_2Sn_6)O_{16}$ (K−Fe), and $K_2(Mn_2Sn_6)O_{16}$ (K−Mn), 2−50 cycles in the voltage range, 0.005−1.0 V. Current density is 60 mA/g for all the compounds. Data for (K−Li) at current rate, 100 mA/g are also shown. Filled and open symbols represent discharge and charge capacities, respectively.

Mg), the difference corresponds to only 0.8 mol of Li, and it is possible that the over-all reaction is not complete during the first-discharge process (Table 2).

The voltage corresponding to the structure destruction is close to that of SnO_2 (∼0.9 V)[1,6,17] but differs from the values observed in tin oxides in glassy matrix (amorphous tin composite oxide (ATCO)) (1.2−1.7 V),[5−7] A_2SnO_4 (A = Mn, Co, Mg; ∼0.9−0.1 V),[17] $ASnO_3$ (A = Ca, Sr, Ba; 0.2−0.3 V),[22] and SnP_2O_7 (1.3 V).[16] Such a variation is attributable to the effect of the crystal structure, counterion, and Sn oxygen coordination. The first-charge profiles comprise a broad voltage plateau region, at ∼0.4 V bounded by small sloping lines for all the Sn-hollandites (Figure 5a). This reaction is essentially a de-alloying process, the reverse reaction in eq 2. First charge capacities (mAh/g) are 505, 602, 481, and 418 for the hollandites (K−Mg), (K−Li), (K−Fe), and (K−Mn), respectively (Table 2 and Figure 5a). These values are lower than the theoretical value of 4.4 mol of recyclable Li/ mol of Sn. These low first-charge capacities are attributed partly to the kinetic reasons and partly to the effect of matrix in not allowing all the inserted Li in the electrode to get extracted during the charge reaction at the employed current densities. This conclusion is supported by the cycling studies on (K−Li) at two different current rates, 60 and 100 mA/g (Figure 6). The capacity values at 100 mA/g are smaller than those obtained when cycled at 60 mA/g.

The voltage versus capacity plots for the hollandites, (K−Li) (current rate = 100 mA/g) and (K−Fe) (current rate = 60 mA/g) in the voltage range of 0.005−1.0 V versus Li up to 50 cycles are shown in Figure 5, panels b and c, respectively. As expected, the second and subsequent discharge profiles differ from the first-discharge profile and correspond to the alloying reaction (forward reaction of eq 2) in an amorphous matrix of K_2O and Li_2O (and Fe for (K−Fe)). The subsequent charge profiles are similar to the first-charge profile (Figure 5a−c). However, the voltage profiles after 10 cycles indicate small electrode polarization and thus, capacity fading with cycling. Average discharge and charge potentials are 0.25 and 0.4 V, respectively, for all the compounds. From Table 2, it is clear that the number

of moles of recyclable Li/mol of Sn is as high as 3.7 for (K−Li) after the 1st charge, which is one of the highest values reported for tin oxides in the literature.[16] The compound (K−Fe) also shows a high value, 3.5 mol of recyclable Li. We note that Fe metal nanoparticles formed during the first-discharge will not participate in the first-charge and subsequent charge−discharge cycles since the upper cutoff voltage is only 1.0 V in our experiments. However, these are expected to act as inert matrix, in addition to K_2O and Li_2O.

The capacity versus cycle number plots for the Sn-hollandites (K−M) at a current density of 60 mA/g in the voltage range of 0.005−1.0 V versus Li up to 50 cycles are shown in Figure 6. For (K−Li) the data at a higher current rate, 100 mA/g, are also presented. The current rate of 60 and 100 mA/g correspond to 0.1 and 0.17 C for (K−Li) assuming 1C = 600 mA/g (equivalent to the observed first-charge capacity). Similarly, for (K−Mg); 1C = 500 mA/g, (K−Fe); 1C = 480 mA/g; and (K−Mn); 1C = 418 mA/g, the current density of 60 mA/g will correspond to 0.12−0.14 C. The charge and discharge capacities for the Sn-hollandites at the 1st, 20th, and 50th cycle along with the equivalent number of moles of Li are given in Table 2. The capacity retention (%) after 50 cycles in each case is also given in Table 2. It is inferred that (K−Li) gives higher capacity values since it has largest number of Sn atoms per formula unit and small Li content with lowest atomic weight. Results from Table 2 and Figures 5b,c and 6 also show that all the Sn-hollandites show capacity fading when cycled up to 50 cycles. The (K−Li) and (K−Fe) retain 78 and 83% of the 1st charge capacity, whereas the (K−Mn) retains only 53% after 50 cycles. As expected, the reversible capacities decreased slightly in (K−Li) when cycled at 100 mA/g in comparison to those observed at the current density of 60 mA/g up to 40 cycles, after which they become identical (Figures 5b and 6 and Table 2). The capacity retention in this case is 85%. It is clear from Table 2 and Figure 6 that the Coulombic efficiency (difference between the charge and discharge capacity at a given cycle number) is >98% in the range of 10−50 cycles in the Sn-hollandites except (K−Mn). The difference in the electrochemical-cycling behavior of (K−Fe) and (K−Mn) is attributed to the poor ability of "Mn" as the matrix element in contrast to "Fe", which effectively buffers the volume variations during cycling. These results are supported by the previous work done on Mn_2SnO_4,[17] $MnMoO_4$,[21] and $NaFeSnO_4$.[23] The Mn as the matrix element in the above showed poor cycling performance while $NaFeSnO_4$ showed excellent cycling response up to 100 cycles with nil capacity fading. We note that the Sn content in the hollandites is much more than the contents of K and M (Li, Mg, Fe, and Mn) ions in the molecular formula $K_2(M\text{-}Sn)_8O_{16}$ and that those elements may not act effectively as the matrix ions in giving stable capacity over large number of cycles. Thus, the cycling performance (50 cycles) of Sn-hollandites compares well with those reported in the literature on other crystalline tin oxides containing $Sn^{4+}O_6$ octahedra except $CaSnO_3$[19] and cubic SnP_2O_7.[16]

3.4. Cyclic Voltammetry of Sn-Hollandites. Cyclic voltammetry can reveal the electrode reactions occurring during cycling and has been used to study the behavior of hollandites (K−Li)and (K−Fe) versus Li at a sweep rate 0.058 mV/s. Figure 7a,b depicts the cyclic voltammograms (CV) as the variation of $|\Delta Q|$(current × time) versus V (volts) in the voltage range 0.005−1.0 and −2.0 V for (K−Li). The curves for (K−Fe) in the range of 0.005−1.0 V are shown in Figure 7c. The first-discharge reaction always commenced cathodically from OCV (∼2.5 V) to 0.005 V. Analogous to galvanostatic cycling profiles, the first-discharge sweep differs significantly from rest of the discharge sweeps. It shows two broad peaks, at ∼0.6 and at ∼0.1 V. The former peak corresponds to the structure destruction and amorphization of (K−Li) and (K−Fe) caused by lithium reaction and formation of Sn metal nanoparticles. Further reaction with lithium leads to the Li−Sn alloy formation depicted by the peak at ∼0.1 V. Subsequent charge-cycles up to 1.0 V (Figure 7a,c) show a peak at ∼0.45−0.55 V, which is indicative of the de-alloying reaction (reverse of eq 2). From the second cycle onward (up to 30 or 40 cycles), the CV up to 1.0 V show only one peak each in the discharge−charge cycle showing the electrochemical cycling of Li via reversible alloy formation. These CV compare fairly well with those observed in $NaFeSnO_4$.[23] The slightly diminishing area of the CV-loops shows gradual capacity fading upon cycling. Figure 7b showing the CV up to 2.0 V cutoff exhibits an additional pair of low-intensity peaks at ∼1.3−1.5 V and at ∼0.65−0.7 V in the anodic (charge) and cathodic (discharge) sweeps, respectively. This is due to the oxidation of Sn during charge sweep and reverting back to metallic Sn during the discharge cycle.[11,20,23] The areas under the main and low-intensity peaks diminish appreciably within 20 cycles, signifying thereby extensive capacity fading when cycled up to ∼2.0 V.

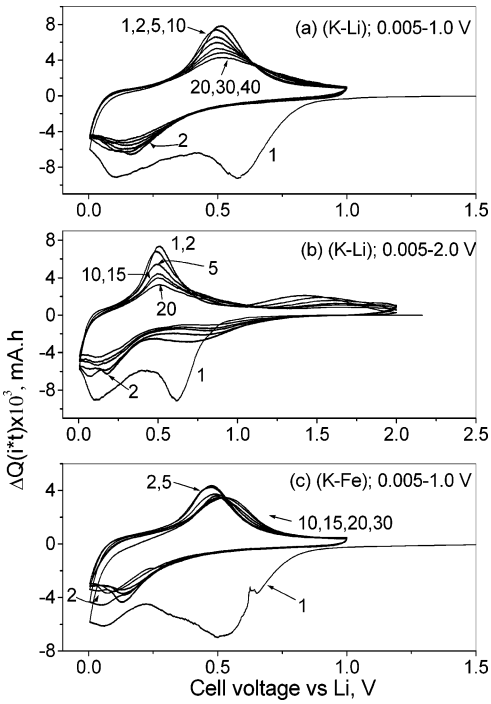

Figure 7. Cyclic voltammograms of $K_2(Li_{2/3}Sn_{22/3})O_{16}$ (K−Li): (a) voltage range 0.005−1.0 V, (b) voltage range 0.005−2.0 V, (c) $K_2(Fe_2Sn_6)O_{16}$ (K−Fe) in the voltage range 0.005−1.0 V. Li metal was the counter and reference electrode. Scan rate was 0.058 mV/s. Only select cycles are shown. Numbers refer to cycle numbers.

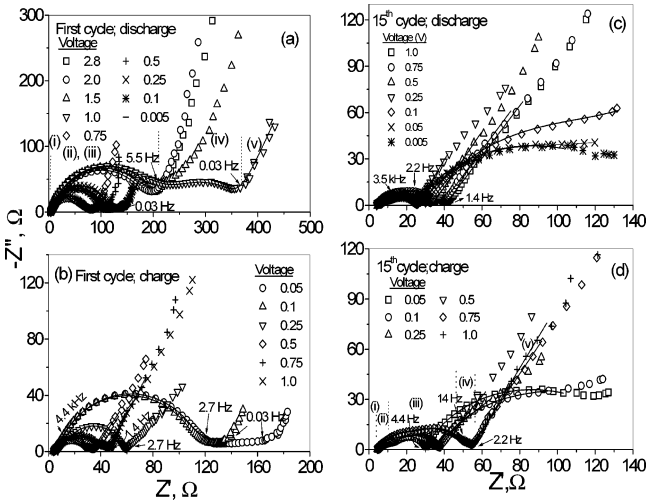

Figure 8. Family of Nyquist plots (Z' vs $-Z''$) for the cell with $K_2(Li_{2/3}Sn_{22/3})O_{16}$ (K−Li) as cathode at different voltages. (a) During the first-discharge reaction from open circuit voltage (OCV = 2.8 V) to 0.005 V (vs Li). (b) During the first-charge reaction from 0.005 to 1.0 V. (c) During the 15th discharge cycle from 1.0 to 0.005 V. (d) During the 15th charge cycle from 0.05 to 1.0 V. Stabilized cell voltages, after 3-h stand, are shown. Select frequencies in the impedance spectra are shown. Regions i−v show fitting with the equivalent circuit of Figure 9.

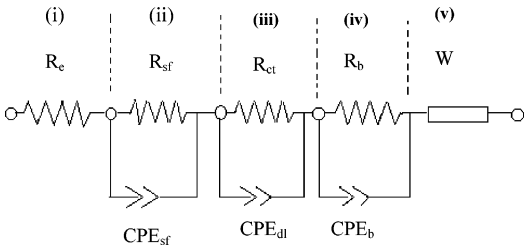

Figure 9. Equivalent circuit used for fitting the impedance spectra of Figure 8. Different resistances, R_i and/or $R_i||CPE_i$ components are shown sectioned as i−iv. Section v is the Warburg element.

Therefore, similar to other tin oxides, for good cycling response, the voltage window is restricted up to 1.0 V in the present study. These CV results complement the galvanostatic cycling response of the Sn-hollandites.

3.5. Electrochemical Impedance Spectroscopy (EIS) of $K_2(Li_{2/3}Sn_{22/3})O_{16}$. 3.5.1. First Discharge−Charge Cycle. EIS was used to study the electrode behavior at different stages of discharge and charge during the 1st and 15th cycle on a cell with $K_2(Li_{2/3}Sn_{22/3})O_{16}$ (K−Li) as the cathode versus Li. The impedance spectra are presented in the form of Nyquist plots (Z' versus $-Z''$) comprising frequency-dependent semicircles and straight line regions in Figure 8. The data were analyzed by fitting with an equivalent circuit made up of resistances R_i, $R_i||CPE_i$ and the Warburg element, W, shown in Figure 9. The CPEs are the constant phase elements that are used to account for the non-homogeneous nature of the composite electrode. The circuit elements are R_e (ohmic resistance of electrolyte and cell components), $R_{sf}||CPE_{sf}$ (impedance of the surface film attributable to the high-frequency semicircle), $R_{ct}||CPE_{dl}$ (charge−transfer impedance due to electrolyte/surface film/electrode interfaces and the double layer (dl) capacitance attributable to the medium-frequency semicircle), $R_b||CPE_b$ (impedance of the bulk composite electrode and bulk capacitance attributable to the low-frequency semicircle), and W, the Warburg impedance governing the diffusion of Li ions at all voltages. Contribution to R_b arises mainly from the electronic resistivity of the active material/matix ions. Various regions in the impedance spectra are shown as sections i−v in Figure 8a,d, and the circuit elements representing these are marked in Figure 9. Symbols represent the experimental data, and the fitting with the equivalent circuit of Figure 9 is shown as continuous lines. The equivalent circuit and the assignment of $R_i||CPE_i$ are in conformity with the recent interpretations of the impedance spectra of the Li-insertion electrodes[36−39] and explains the high effective values of the observed CPE_b, which are in the range of mF.[38,39] It may be mentioned that since major changes occur in the (K−Li) during the cycling process in comparison to those at the counter (Li-metal) electrode, the variations in the impedance spectra and relevant parameters as a function of voltage can be safely attributed to the test electrode of the two-electrode cell.

Family of Nyquist plots for the first-discharge cycle from OCV to 0.005 V at various intermediate potentials is presented in Figure 8a. The fitted values of the impedance parameters are given in Table 3. For the spectra comprising a single semicircle followed by a straight line (i.e., in the voltage range OCV (2.8)−1.5 V and 0.25−0.005 V, the circuit without R_b, CPE_b, and W was used for the fitting. Fitting was not done in the low-frequency region (<0.1 Hz) since the curves were not fully developed.

According to the fitting, in all the Nyquist plots, the R_e (ohmic resistance of the electrolyte and cell components) is 2−4 (± 0.5) Ω, indicating that the cells have been properly fabricated. The single semicircle in the high-medium-frequency range in the spectra at 2.8, 2.0, and 1.5 V (Figure 8a), corresponding to a resistance of ∼210 Ω, can be attributed to the overall impedance, comprising the surface film and the charge-transfer resistance ($R_{sf} + R_{ct}$). The straight-line portion in the low-frequency region (<5.5 Hz) represents the Warburg-type region for a nonideal electrode system.[40−45]

The impedance spectrum at 1.0 V comprises an additional depressed semicircle. This is indicative of additional impedance that can therefore be ascribed to the bulk resistance of the composite electrode (R_b = 120 (± 5) Ω with the associated CPE_b = 4 (± 1) mF). The spectrum at 0.75 V (and at 0.5 V), where the diameter of the first-semicircle decreased to ∼78 Ω and the second semicircle representing R_b disappears (Figure 8a), shows that the overall electrode impedance decreased extensively due to the formation of

(36) Nobili, F.; Croce, F.; Scrosati, B.; Marassi, R. *Chem. Mater.* **2001**, *13*, 1642.
(37) Nobili, F.; Tossici, R.; Croce, F.; Scrosati, B.; Marassi, R. *J. Power Sources* **2001**, *94*, 238.
(38) Levi, M. D.; Aurbach, D. *J. Phys. Chem. B* **2004**, *108*, 11693.
(39) Nobili, F.; Dsoke, S.; Croce, F.; Marassi, R. *Electrochim. Acta* **2005**, *50*, 2307.
(40) Sharma, N.; Shaju, K. M.; Subba Rao, G. V.; Chowdari, B. V. R. *Electrochim. Acta* **2004**, *49*, 1035.
(41) Sharma, N.; Subba Rao, G. V.; Chowdari, B. V. R. *Electrochim. Acta* (in press).
(42) Sharma, N.; Deepa, M.; Agnihotry, S. A. *Solid State Ionics* **2002**, *152−153*, 873.
(43) Levi, M. D.; Aurbach, D. *J. Phys. Chem. B* **1997**, *101*, 4630.
(44) Aurbach, D.; Nimberger, A.; Markovsky, B.; Levi, E.; Sominski, E.; Gedanken, A. *Chem. Mater.* **2002**, *14*, 4155.
(45) Reddy, M. V.; Madhavi, S.; Subba Rao, G. V.; Chowdari, B. V. R. *Chem. Mater.* (submitted).

Table 3. Impedance Parameters Extracted by Fitting the Spectra to the Circuit Elements during Discharge and Charge Cycle for $K_2(LiSn)_8O_{16}$ (K−Li)

voltage, V (vs Li)	R_{sf} (±2 Ω)	R_{ct} (±5 Ω)	R_b (±2 Ω)	CPE_{sf} (±5 μF)	CPE_{dl} (±5 μF)	CPE_b (±1 mF)
			First Discharge			
2.8−1.5	210	$R_{sf} + R_{ct}$	nil	30	$CPE_{sf} + CPE_{dl}$	
1.0	238		120	27		4
0.75−0.5	78−65		nil	22		
0.25	116		19	37		
0.1−0.005	100		39	30		
			First Charge			
0.05	5	107	68	78	25	
0.1	5	105	16	80	25	
0.25	8	46	nil	22	43	
0.5	13	10	9	94	41	11
0.75		36	3		90	8
1.0		32	6		78	3
			15th Discharge			
1.0	16	11	7	60	160	1.5
0.75	17	11	4	61	160	2
0.5	16	10	3	64	150	5.5
0.25	11	10	1.6	73	160	16
0.1	10	17	111	47	190	119
0.05	10	12	105	77	150	84
0.005	9	12	116	97	129	50
			15th Charge			
0.05	12	18	82	59	135	72
0.1	13	18	80	61	135	74
0.25	14	16	15	75	180	70
0.5	18	12	2	70	150	8.5
0.75	22	20	2.5	44	130	5
1.0	22	22	4	50	137	3.5

more conducting tin nanoparticles as a result of structure destruction (Eqn.1). This is the region in which Sn and Li_xSn coexist in equilibrium. However, the increase in the diameter of the first semicircle by ∼40 Ω (fitted value is 116 Ω) in the spectrum at 0.25 V and the accompanying very-depressed semicircle (almost like a horizontal line) shows an increase in ($R_{sf} + R_{ct}$) accompanied with the re-occurrence of R_b at this voltage (Figure 8a). This can be ascribed to the almost single-phase alloying reaction represented by the sloping region of the galvanostatic first discharge profile (Figure 5a and eq 2). Actually, the first-discharge reaction is the "electrode formation cycle", and the time constants corresponding to various processes are inseparable and thus cannot be identified clearly. The Nyquist plots at subsequent discharge potentials 0.1 and 0.005 V are almost identical to that measured at 0.25 V. Corresponding CPEs at all voltages are in the range of, 22−37 (± 5) μF (Table 3).

The Nyquist plots for the first-charge cycle from 0.005 to 1.0 V are shown in Figure 8b. The spectra at all voltages showed evolution of an additional small semicircle in the high-frequency region (0.35 MHz−5 kHz) attributable to the impedance of surface film (R_{sf}) (i.e., impedance of SEI similar to the ones reported in the literature).[36−41,43−49] The fitted values ranged from 5 to 13 (± 2) Ω (Table 3). At 0.05 and 0.1 V, the R_{ct} represented by the second depressed semicircle in the intermediate frequency range 4.4 kHz−2.7 Hz is 106 (± 5) Ω, and the R_b is represented by depressed semicircle (seen as almost a straight line) in the frequency range of 2.7−0.03 Hz. The charge reaction till 0.25 V caused R_{ct} to decrease to 46 (± 5) Ω (CPE_{dl} = 43 μF), and the R_b was reduced to negligible values (Table 3). This decreasing trend of ($R_{sf} + R_{ct}$) is seen till 0.5 V. Moreover, at this voltage as well as at 0.75 V, three overlapped semicircles are seen, representing time-dependent impedances due to SEI (R_{sf}) (0.35 MHz−4.4 kHz), charge transfer (R_{ct}) (4.4 kHz−35 Hz), and bulk (R_b) (35−1.4 Hz). This voltage range matches well with the plateau region 0.25−0.5 V observed during the first-charge reaction in the galvanostatic profile, where Sn and Li_xSn are coexisting in equilibrium and thus offering minimum impedance to Li ion extraction. Subsequent charge reaction up to 0.75 and 1.0 V led to a slight increase in the R_{ct} to 31(± 5) Ω and R_b to 4(± 2)Ω, since in this voltage range, the dealloying reaction is completed. We observed a significant decrease in the R_b and R_{ct} in the case of $CaWO_4$[41] upon Li extraction, although the reaction mechanism in this case is of redox-type.

3.5.2. Impedance Spectra during the 15th Discharge−Charge Cycle. The first discharge−charge cycle is the "formation cycle" involving both eqs1 and 2, whereas the subsequent cycles involve only eq 2 and contribute to the reversible capacity. Furthermore, from Figure 6 it is clear that the Coulombic efficiency attains maximum value only after the first few discharge−charge cycles. Hence, EIS studies were carried out during the 15th discharge−charge cycle (0.005−1.0 V), and the Nyquist plots are shown in Figure 8c,d, respectively. Qualitatively, the spectra are similar at a given voltage thereby showing good electrochemical reversibility.

The first semicircle in the high-frequency region (0.35 MHz−3.5 kHz; section ii) gave R_{sf} = 13 ± 4 and 16 ± 6 Ω

(46) Li, H.; Huang, X.; Chen, L. *J. Power Sources* **1999**, *81−82*, 340.
(47) Kang, Y.-M.; Kim, K. T.; Lee, K.-Y.; Lee, S.-J.; Jung, J.-H.; Lee, J.-Y. *J. Electrochem. Soc.* **2003**, *150*, A1538.
(48) Wachtler, M.; Besenhard, J. O.; Winter, M. *J. Power Sources* **2001**, *94*, 189.
(49) Dolle, M.; Poizot, P.; Dupont, L.; Tarascon, J.-M. *Electrochem. Solid-State Lett.* **2002**, *5*, A18.

during the 15th discharge and charge cycle, respectively, indicating almost nil voltage dependence (Table 3 and Figure 8c,d). The corresponding CPE_{sf} are in the range of 59−97 (± 5) μF. These potential independent values of impedance reflect the stability of SEI with the depth of discharge/charge. The stable SEI in turn prevents further decomposition of the electrolyte at the electrode−electrolyte interface up on electrochemical cycling. Similar results were reported on other Li-insertion electrodes.[36,37,39,41,45]

The spectra in the voltage range of 1.0−0.25 V during both 15th charge and discharge cycle comprise two overlapped semicircles in the intermediate frequency range of 3.5 kHz−1.4 Hz and correspond to sections iii and iv of Figure 9 representing $R_{ct}||CPE_{dl}$ and $R_b||CPE_b$ circuit elements, respectively. The low-frequency Warburg region, a straight line with a slope of 50−55°, is clearly delineated. However, for $0.25 < V \leq 0.005$ V, the $R_b||CPE_b$ component extends to low-frequency region (2.2 Hz−2 mHz), and the Warburg region is not seen due to experimental limitation. The fitted values of impedance parameters given in Table 3 show an interesting trend in R_{ct} and R_b. Both of them go through a minimum in the voltage range of 0.25−0.50 V, the region of coexistence of Sn and $Li_{4.4}Sn$ phases along with the Li-M−O matrix. Interestingly, the R_b values (and the CPE_b) increase by more than an order of magnitude under deep discharge conditions, 0.1 → 0.005 V (Table 3). This shows that as more and more of the alloy ($Li_{4.4}Sn$) forms from the nano-metal Sn particles, bulk impedance, and to a smaller extent, the charge−transfer impedance (R_{ct}) increase. This is to be expected since the alloy will have a higher absolute value of resistivity as compared to Sn-metal. Indeed, the recent single crystal study on Li−Sn alloy system has shown that the actual composition is $Li_{4.25}Sn$ and not $Li_{4.4}$-Sn as usually envisaged, and it is a poor metal.[50] A closer look at the R_{ct} value at 1.0 V during the discharge and charge operation shows that it increased from 11 to 22 (± 5) Ω. This increase, along with the large variations in R_b during either charge or discharge sequence may be the reason for the observed capacity fading in (K−Li) on cycling to 50 cycles.

4. Summary and Conclusions

Tin oxides with the hollandite structure, $K_2(M,Sn)_8O_{16}$, M = metal, have been investigated as possible anodes for LIB. These contain electrochemically active SnO_6 octahedra, and the K and M metals act as the matrix (spectator) ions. The compounds $K_2(Li_{2/3}Sn_{22/3})O_{16}$ (K−Li), $K_2(Mn_2Sn_6)O_{16}$ (K−Mn), and $K_2(Fe_2Sn_6)O_{16}$ (K−Fe) are new isostructural phases. These along with $K_2(MgSn_7)O_{16}$ (K−Mg) have been synthesized and characterized by XRD, SEM, XPS, and BET surface area. Rietveld refinement of the powder XRD data yielded the nominal composition, tetragonal lattice parameters, and occupancies of the ions with good fitting. XPS on (K−Li) and (K−Mg) confirm the formal valencies of the ions in the compounds. Galvanostatic charge−discharge cycling, at 60 (and 100) mA/g in the range of 0.005−1.0 V versus Li metal up to 50 cycles, cyclic voltammetry (CV) and impedance spectroscopy were carried out on cells at ambient temperature.

Crystal structure destruction occurs during the first-discharge (reaction) with Li, followed by reduction to Sn-metal and Li_xSn alloy formation. Subsequent charge−discharge cycling involves a de-alloying−alloying reaction of Li_xSn in the amorphous/nano-crystalline matrix of Li−M−O and contribute to the reversible capacity. The first-charge capacities shown by (K−Li), (K−Mg), (K−Fe), and (K−Mn) are 602, 505, 481, and 418 (± 3) mAh/g respectively, which correspond to 3.7−3.0 mol of recyclable Li/mol of Sn (theoretical, 4.4 Li). Slow degradation of the capacity was noted in all cases. However, (K−Li) and (K−Fe) performed better and retained 78 and 83% of the initial capacity respectively after 50 cycles. (K−Mg) and (K−Mn) retained only 68 and 53% of the initial capacity under the above conditions. This clearly indicates the effect of matrix metal/ion on the Li-recyclability. The average charge and discharge voltages were found to be 0.4−0.5 and 0.25−0.30 V, respectively, with Coulombic efficiency >98% in all cases except (K−Mn) in the range of 10−50 cycles. The CV data complement the galvanostatic cycling results and showed that a good operating voltage range is 0.005−1.0 V versus Li.

Impedance spectral data, measured on cells with (K−Li) during the 1st and 15th cycle at various voltages, have been fitted to an equivalent circuit; the relevant parameters were evaluated. Results show that while the surface film resistances (R_{sf}) does not vary much with the voltage, the charge-transfer resistance (R_{ct}) and bulk resistance (R_b) go through a minimum in the voltage range of 0.25−0.50 V, the region of coexistence of Sn and $Li_{4.4}Sn$ phases along with the Li−M−O matrix. Interestingly, the R_b values (and the capacitance, CPE_b) increase by more than an order of magnitude under deep discharge conditions, 0.1 → 0.005 V. This shows that as more and more of the alloy ($Li_{4.4}Sn$) forms from the nano-metal Sn particles, bulk impedance and to a smaller extent the charge-transfer impedance (R_{ct}) increase. The latter two effects possibly contribute to the observed capacity fading in (K−Li) and other Sn-hollandites.

The electrodic-performance of the Sn-hollandites compares well with that reported on other tin oxides with the $Sn^{4+}O_6$ octahedra, except $CaSnO_3$ and cubic-SnP_2O_7. We conclude that studies on crystalline Sn-mixed oxides need to be continued to arrive at the optimum crystal structure, matrix atoms/ions, and their content for use in LIB.

Acknowledgment. Thanks are due to Ms. Liu Yan, Surface Science Laboratory, Department of Physics, NUS, for help in collecting XPS data.

CM0505042

(50) Lupu, C.; Mao, J.-G.; Rabalais J. W.; Guloy, A. M.; Richardson, J. W. *Inorg. Chem.* **2003**, *42*, 3765.